ELSEVIER

Endwall heat transfer measurements in an annular cascade of nozzle guide vanes at engine representative Reynolds and Mach numbers

M. C. Spencer and T. V. Jones
Department of Engineering Science, University of Oxford, UK

G. D. Lock *
School of Mechanical Engineering, University of Bath, UK

Aerodynamic and heat transfer measurements have been made on the hub and casing endwalls of a large (mean diameter 1.1 m) annular cascade of high-pressure nozzle guide vanes. The measurements have been made over a range of engine representative Mach and Reynolds numbers and with large levels of free-stream turbulence intensity. The transient liquid crystal technique has been employed, which has the advantage of yielding full surface maps of heat transfer coefficient. Aerodynamic measurements of Mach number distributions on the end-wall surfaces are also presented, along with surface-shear flow visualisation using oil and dye techniques. The heat transfer results are discussed and interpreted in terms of the secondary flow and Mach number patterns.

Keywords: heat transfer; annular cascade; nozzle guide vane; liquid crystals

Introduction

There is a general need to increase peak turbine temperatures in future gas turbine aeroengines in order to offer improved performance. Experimental measurements of heat transfer to the endwalls of the first stage nozzle guide vane downstream of the combustor provide information to aid the engine designer and to validate computational codes. The heat flux to these endwalls is highly nonuniform and influenced by the presence of complex three-dimensional (3-D) secondary flows.

A comprehensive review of the experimental and computational research on annular nozzle guide vane (NGV) cascade endwalls has been presented by Harvey and Jones (1990). Measurements of heat transfer at engine representative Reynolds and Mach numbers have been reported by several authors (Chana 1992; Harasgama and Wedlock 1990; Harvey and Jones 1990; Kingcombe et al. 1989). Generally these researchers have all identified high heat transfer levels at the leading and trailing edge regions of the NGV and significant cross-passage heat transfer gradients. In all cases reported, the measurements have been obtained using thin film methods (Schultz and Jones 1977), which have a limited spatial resolution due to the finite number of gauges that can be realistically placed on the endwalls. Furthermore, these gauges have an inherent spatial limitation, as each has a finite size and yields an average measurement over its area. This limitation is particularly severe in regions of high spatial gradients of heat transfer, which are often the areas of most interest.

In the work reported here, the transient liquid crystal technique has been employed as a means of measuring the heat transfer levels. The advantage of this method is that accurate maps of heat transfer coefficient can be generated over the entire surface without the constraints of limited spatial resolution. In regions of large heat transfer gradients, the applied technique is particularly advantageous, as thin film gauges cannot a priori be positioned in these regions.

This paper describes the use of liquid crystals in a cold heat transfer tunnel (Harvey et al. 1989; Martinez-Botas et al. 1993) and presents global maps of heat transfer coefficient on the end-wall surfaces. These measurements have been made in a large annular cascade of nozzle guide vanes at engine representative Reynolds and Mach numbers. The free-stream turbulence intensity levels and length scales have been measured using a hot-wire anemometer and are also engine representative. The heat transfer measurements are complemented with measurements of the Mach number distribution on the end-wall surfaces and with surface-shear flow visualisation using oil and dye techniques.

* Visiting Lecturer, University of Oxford

Address reprint requests to Dr. G. D. Lock, Department of Engineering Science, University of Oxford, Parks Road, Oxford OX1 3PJ, UK.

Received 26 June 1995; accepted 11 November 1995

Int. J. Heat and Fluid Flow 17: 139–147, 1996

655 Avenue of the Americas, New York, NY 10010

0142-727X/96/$15.00
SSDI 0142-727X(95)00102-6

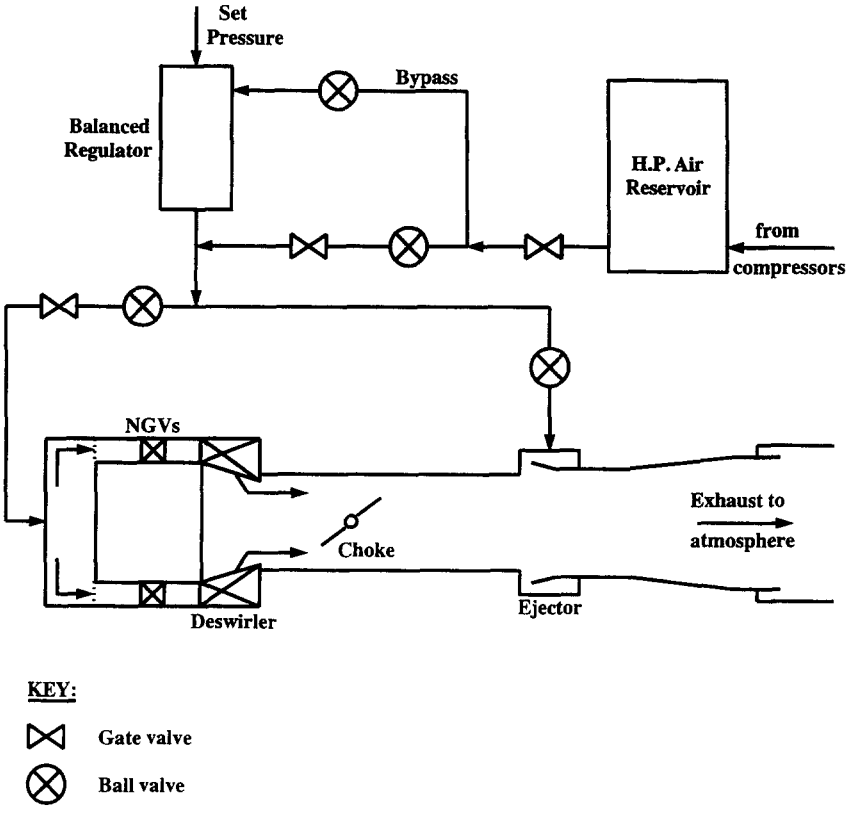

Figure 1 Schematic diagram of the Cold Heat Transfer Tunnel

Experimental technique and test facility

The transient liquid crystal technique has been well established at Oxford and elsewhere. The NGV surface temperature is monitored using thermochromic liquid crystals as it is subjected to a step change in convective heating. This leads to measurements of the heat transfer coefficient h

$$\dot{q} = h(T_{gas} - T_s) \tag{1}$$

where T_{gas} and T_s are the gas and surface temperatures, and $\dot{q}$ is the heat flux per unit area. This technique has been used in a transonic situation. It is, therefore, necessary to use the recovery or adiabatic wall temperature as T_{gas} in the above equation. This temperature was obtained assuming a recovery factor r equal to 0.89 (taken as the Prandtl number raised to the 1/3 power, Kays and Crawford 1993), and using the relationship between the local Mach number and the adiabatic temperature; namely,

$$T_{gas} = T_\infty\left(1 + r\frac{\gamma - 1}{2}M_\infty^2\right) \tag{2}$$

In this equation, T_∞ and M_∞ are the local temperature and Mach number.

The measurements were performed in the Oxford University Cold Heat Transfer Tunnel (Martinez-Botas et al. 1993, 1995), or CHTT. The test section of the tunnel is an annular cascade of 36 NGVs at 1.4 times larger than engine scale. The test duration of the facility (about 7 seconds at the engine design condition) enables transient techniques to be employed. The tunnel allows an independent variation of Reynolds and Mach numbers, or equivalently the upstream and downstream pressures can be independently and continuously varied.

A schematic diagram of the CHTT is shown in Figure 1, and details of the nozzle guide vanes are summarised in Table 1. The operation of the tunnel is controlled by pneumatically activated ball valves. Air flows from the high-pressure reservoir (31 m^3 at 3 MPa) into a regulator system from which part of the flow enters an ejector. The remainder passes into the annular test section containing the NGVs, subsequently exhausting to atmosphere. Large levels of turbulence are created using a resistance plate upstream of the cascade with an open area of 9%.

Notation

c	specific heat capacity
c_{ax}	axial chord
h	heat transfer coefficient
k	thermal conductivity
M	Mach number
Nu	Nusselt number, based on axial chord
$\dot{q}$	heat flux
r	recovery factor
Re	Reynolds number, based on axial chord
T	temperature
Tu	turbulence intensity

Greek

ϵ	uncertainty, %
Λ	turbulence length scale
ρ	density
ω	wave number

Table 1 Nozzle guide vane details

Midspan axial chord (c_{ax})	0.0664 m
Mean pitch at exist	0.09718 m
Span at exit	0.08076 m
Turning angle	73 °
Throat area	0.08056 m^2
Mean blade diameter	1.113 m

Two shutters are used to isolate five transparent, perspex blades enclosing four complete blade passages and endwalls in the annulus. These blades and shutters form a *cassette* (Figure 2), which can be inserted into the annulus and preheated. The shutters are removed in less than 70 ms during tunnel operation and create the required step change in heat transfer. It should be noted that any transient effects of gas temperature and velocity are essentially isolated from the test vane by the shutters, which only open when steady conditions prevail. The design and operation of this cassette are discussed in a previous paper (Martinez-Botas et al. 1995).

In the tests described in this paper, the end-wall surfaces of the central perspex blade in the cassette were coated with two thermochromic liquid crystals. The crystal temperatures chosen were 25 and 30 C, the initial preheated temperature was 65 C, and this was uniform within 2 C around the NGV before the experiment. The free-stream stagnation temperature was typically 12 C, and the local gas recovery temperature varied between 2 and 12 C over the NGV surface under engine design flow conditions.

The liquid crystal colour changes, measured from when the shutters open, were viewed using miniature CCD cameras and recorded on video. The perspex endwall is transparent, and the crystals lie underneath a thin coating of black paint. The cameras are located outside the tunnel to view the casing, and access is available inside the annulus to view the hub endwall. Surface markings, painted on the blade surface, were used as a grid. Virtually all of the end-wall surfaces were visible to the cameras, but small portions of the image were obscured by bolt holes. The video images, recorded at 25 frames per second, were analysed using an advanced digital image-processing system developed at Oxford (Wang 1991) to obtain light intensity plots at all points of interest.

It should be noted that different parts of the model subtended a range of angles at the camera during the test. The effect of angle on perceived colour is relatively small for encapsulated narrow-band liquid crystals. This was checked during the calibration of the liquid crystals for these tests. The uncertainty in the heat transfer measurements using the liquid crystals is discussed in detail in the appendix.

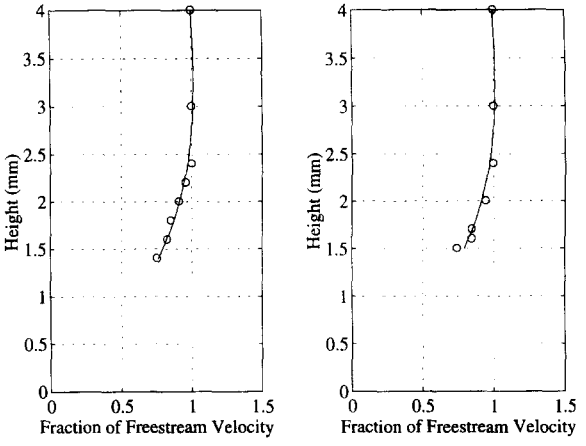

Figure 3 (a) Casing boundary-layer profile (left); (b) Hub boundary-layer profile (right)

Cascade inlet and exit conditions

A hot-wire boundary-layer probe was used to measure the upper part of the boundary-layer profile approximately three axial chords upstream of the NGV leading-edge plane. This position is roughly two axial chords upstream of the contraction (area ratio of 1.7) leading to the NGVs, and the survey was carried out on both the hub and casing endwalls. A micrometer screw adjustment was used to locate the probe within the tunnel. The results are shown in Figures 3 and 3b, which illustrate a boundary layer (expected to be turbulent) with a thickness of approximately 2.5 mm.

A hot-wire anemometer was used to measure the flow velocity, integral length scale (Λ), and turbulence intensity (Tu) across the span in the leading-edge plane of the NGVs. Results of this survey are shown in Figure 4. The flow velocity is seen to be fairly uniform across the span (mean value 57 m/s), and the average turbulence intensity and integral length scale are 13% and 21 mm, respectively. The turbulence integral length scale

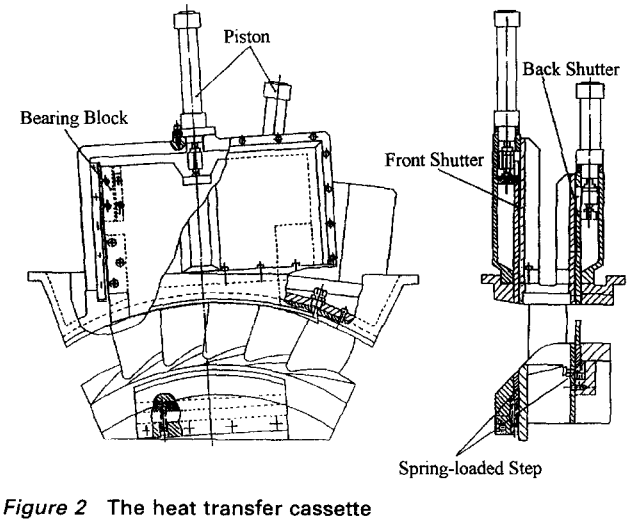

Figure 2 The heat transfer cassette

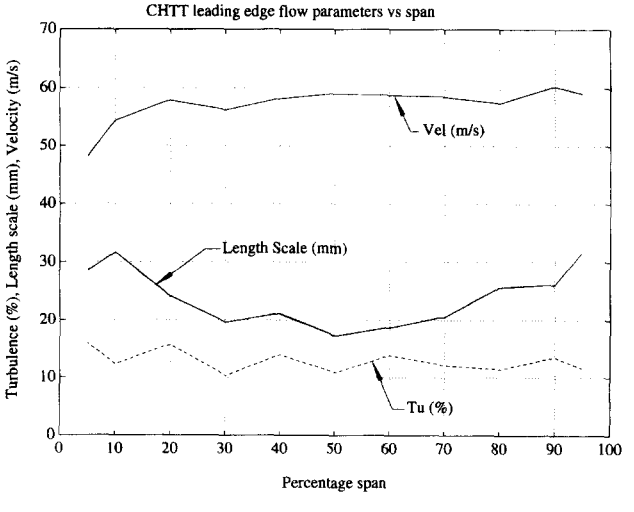

Figure 4 Turbulence characteristics at nozzle guide vane inlet

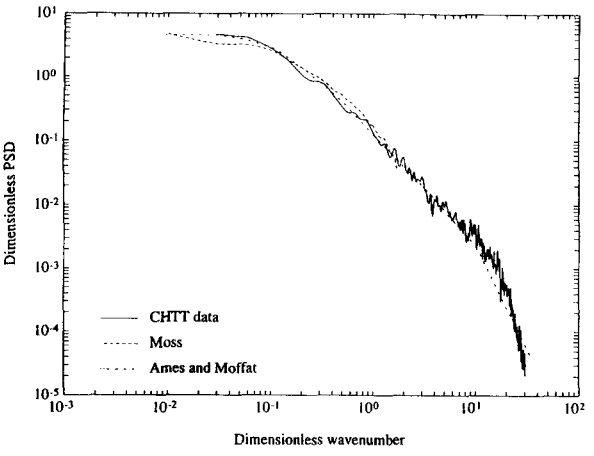

Figure 5 Turbulence spectra comparision

was obtained using a standard autocorrelation (Hinze 1975) and is the order of that expected in an aeroengine, the length scale being determined by the dilution hole diameter in the combustor (Moss and Oldfield 1991).

The high levels of turbulence are created in the tunnel due to the presence of the resistance plate upstream of the NGVs. Figure 5 compares the shape of the measured turbulence spectrum in the CHTT with that measured from a simulated combustor chamber (Ames and Moffat 1990) and from a gas turbine aeroengine combustor (Moss and Oldfield 1991). The data have been plotted on nondimensional axes to allow comparison. The dimensionless wave number is equal to $\Lambda\omega/2\pi$, and the dimensionless power spectral density is $2\pi[Tu^2\Lambda]$PSD, where ω and PSD are the conventional wave number and power spectral density, respectively. These spectra are seen to be similar, and the turbulence levels and length scales are of the same order as those expected in an aeroengine.

Table 2 Exit flow conditions

Condition	Mach number	Reynolds number
Design	0.96	1.9×10^6
Mach plus	1.1	1.9×10^6
Mach minus	0.82	1.9×10^6

Table 3 (Cold heat transfer tunnel) engine comparison

Parameter	Engine	CHTT
Inlet total pres, bar	32	2
Turbine inlet temp, K	1750–1800	290
Blade/gas_{max}temp	0.58	0.8–1.15
Exit Re no, c_{ax}	2×10^6	2×10^6
Exit Mach no	0.96	0.96
Peak Nu no	3500	3500
Peak h, $Wm^{-2}K^{-1}$	8400	1300
Mass flow rate, kg/s	120	38

The tunnel exit conditions were monitored using end-wall static pressure tappings located half an axial chord downstream of the NGV trailing edge. The isentropic exit Mach number is based on an average between the hub and casing static pressures, and the exit Reynolds number is based on this Mach number and the axial chord. Three exit Mach numbers were employed in the CHTT, each at the same Reynolds number. The test conditions are summarised in Table 2.

A comparison between conditions in a typical modern aeroengine and the CHTT is summarised in Table 3. The CHTT does not model the engine blade-to-gas temperature ratio. The influence of this temperature ratio on heat transfer mainly enters as gas property variations through the boundary layer. This influence is well documented for both laminar and turbulent boundary layers (Fitt et al. 1986). A secondary influence is through the

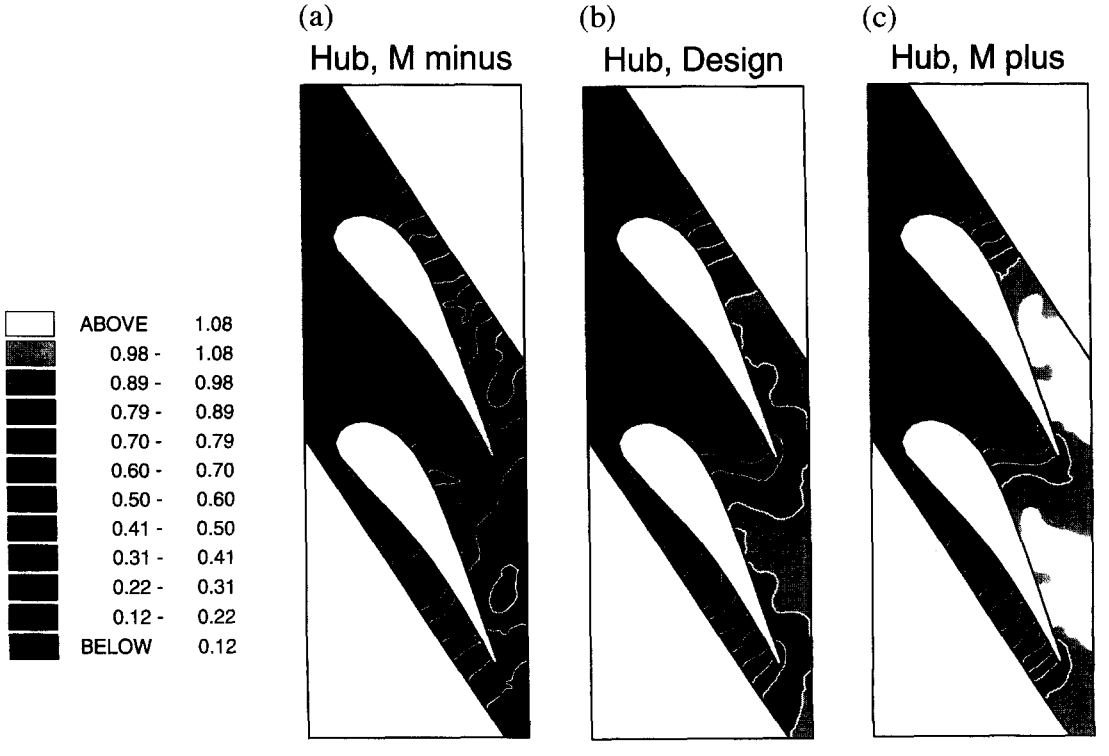

Figure 6 Isentropic Mach number contours on the hub endwall: (a) Mach minus; (b) design; (c) Mach plus

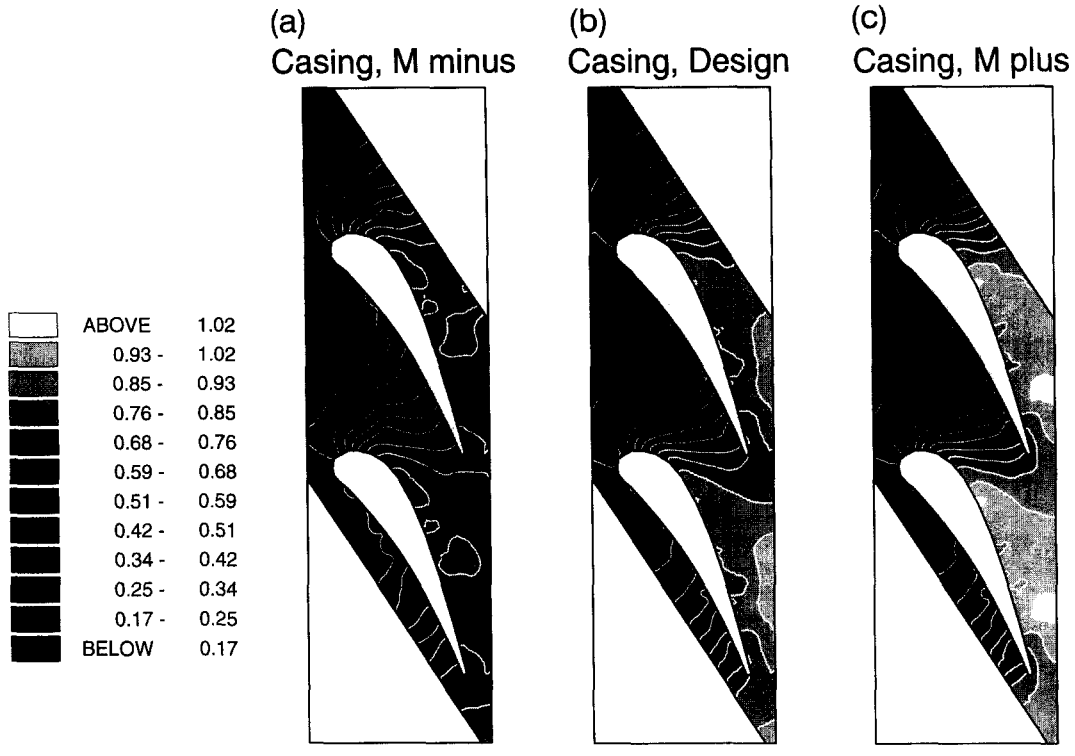

Figure 7 Isentropic Mach number contours on the casing endwall: (a) Mach minus; (b) Design; (c) Mach plus

stability of the laminar boundary layer and, hence, the transition point. However, above free-stream turbulence levels of 1–2%, the transition is via a bypass mechanism, and, hence, at the large levels of turbulence in the tests reported here, the gas-to-blade temperature ratio would be expected to have no influence. This has been demonstrated experimentally in the CHTT by measuring identical heat transfer coefficients for both precooled and pre-heated blades (Guo et al. 1995). The tests, therefore, represent engine conditions well in that transition is not influenced and property effects may be taken into account.

Experimental Mach number distribution

Examination of Equation 2 reveals that it is necessary to know the local Mach number at any surface position in order to calculate the gas recovery temperature and, hence, the heat transfer coefficient. To measure the local Mach number, two NGVs were instrumented with hub and casing end-wall static pressure tappings (56 tappings on the hub and 59 on the casing endwall). From data measured using these tappings, contours of local isentropic Mach number have been plotted for both end-wall surfaces at the three flow conditions. These are shown as Figures 6 and 7.

These Mach number contours are useful in interpreting the heat transfer contours (shown below). It is apparent from these figures that there is very little effect of a varying exit Mach number on local Mach number in regions where the flow can be considered to be incompressible (i.e., toward the leading edge of the vane). However, in regions of compressible flow (from about 50% axial chord and beyond), there is an expected variation, with local Mach numbers being higher for the Mach plus condition and lower for the Mach minus condition. The highest Mach numbers can be found on the late suction surface side of the endwall, and the Mach numbers on the hub are higher than those on the casing as radial equilibrium dictates a lower hub static pressure.

Flow visualisation

Surface-shear flow visualisation experiments were performed in the CHTT to aid in interpretation of the heat transfer measurements. The results are shown in Figures 8 and 9 and were obtained using a mixture of silicone oil and paraffin with coloured fluorescent dye. Following Harvey (1991), the vane aerofoils and endwalls downstream of the leading edge were painted one colour (which shows lighter in the figures). Upstream of the vane leading edge, the endwalls were painted another colour (which shows up darker in the figures). The penetration of the second dye into the passage during the run clearly illustrates the secondary flow patterns.

The formation of secondary flows in turbine passages are well documented (Sieverding 1985; Langston 1989). Figure 10 is a diagrammatic representation of turbine secondary flows (Takeishi et al. 1989). The complexity of secondary flows makes their

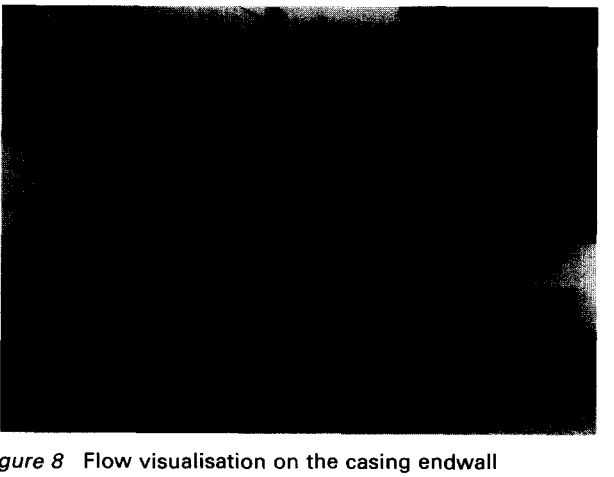

Figure 8 Flow visualisation on the casing endwall

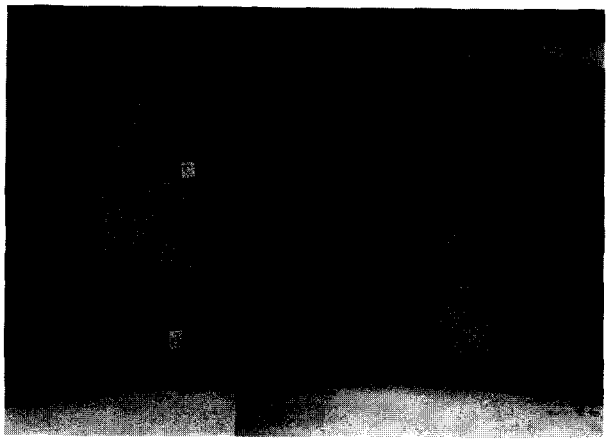

Figure 9 Flow visualisation on the aerofoil suction surface

detailed representation difficult, and this figure provides a useful simplification. The principal features are as follows. First, a rolling up of the inlet boundary layer into the horseshoe vortex. The pressure side leg of this becomes the core of the passage vortex. The passage vortex is the dominant part of the secondary flow, and beneath this on the endwall a new boundary layer is formed. The deflection of this new boundary layer across the passage is referred to as downstream cross-flow 2 in Figure 10. Second, upstream of this, the inlet boundary layer is deflected across the passage and referred to as upstream cross flow 1. The end-wall separation line marks the farthest penetration of the bottom of the inlet boundary layer into the passage and divides it from the new boundary layer forming downstream of it. Third, the new end-wall boundary layer, cross-flow 2, carries up onto the aerofoil suction surface until it separates (along the vane separation line c, see also Figure 9) and feeds into the passage vortex. The suction leg of the horseshoe vortex, referred to as the counter vortex in Figure 10, remains above the passage vortex and moves away from the endwall as the passage vortex grows.

The principal features of secondary flow have been identified using flow visualisation experiments. The separation lines on the casing endwall are shown in Figure 8. The pressure and suction surface legs are marked as *a* and *b*. These lines mark the farthest penetration of the bottom of the inlet boundary layer into the passage. Upstream of the separation line, the flow is seen to migrate across the passage to the suction surface (cross-flow 1) and lines *a* and *b* converge along the aerofoil to make a separation line *c*. This latter line is shown in Figure 9, which is a view of the aerofoil suction surface. The line *d* in this figure is the separation line from the flow over the hub endwall. This line runs much closer to the endwall because of the radial pressure gradient.

Light dye (in Figure 8) is seen to have migrated upstream from the leading edge onto the casing endwall by the formation of the horseshoe vortex. The suction-side separation line *b* on the casing endwall passes around the leading edge before it sweeps up onto the suction aerofoil surface. The corresponding separation line on the hub is seen to sweep up onto the aerofoil surface in the leading edge region, much closer to the stagnation point. This is because the flow at the hub has been accelerated through a steep contraction (see the cross section in Figure 2) and contains a radial component of velocity and pressure gradient at the leading edge plane. This hub-to-casing velocity has been identified in this region with the oil flow visualisation. This results in the horseshoe vortex being lifted off the hub endwall much closer to the stagnation point than the horseshoe vortex on the casing.

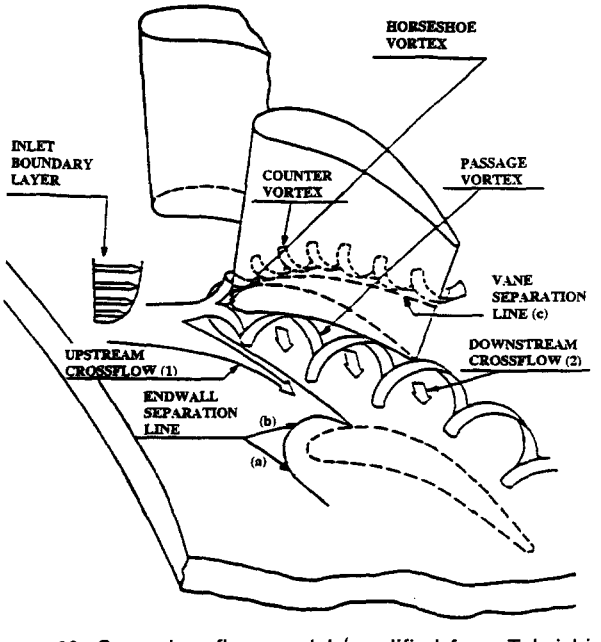

Figure 10 Secondary flow model (modified from Takeishi et al. 1989)

Heat transfer data and discussion

Figure 11 shows the variation of the perspex temperature on the NGV surface as well as the stagnation gas temperature during a typical run of the CHTT. These measurements are made using thermocouples located on the vane surface and in the gas upstream of the test section. As the tunnel starts, cold air leaks into the enclosed volume of the cassette causing a slight drop in the initial surface temperature before the shutters open. The times for the shutters to begin and complete their operation were measured using microswitches. This deployment time was less than 70 ms and is shown in the figure. The free-stream temperature is seen to vary between 12.5 and 10 C during the 4 seconds of regulated steady flow. The initial peak is due to compression heating during the tunnel startup procedure.

Figures 12 and 13 show global contours of experimentally deduced heat transfer coefficient for the hub and casing endwalls at the three engine representative conditions. Superimposed on the contours at the design condition (Figures 12b and 13b) are the separation lines from the flow visualisation experiments. The figures are a projection of the curved end-wall surfaces onto a two-dimensional (2-D) plane. Hence, in the regions of high

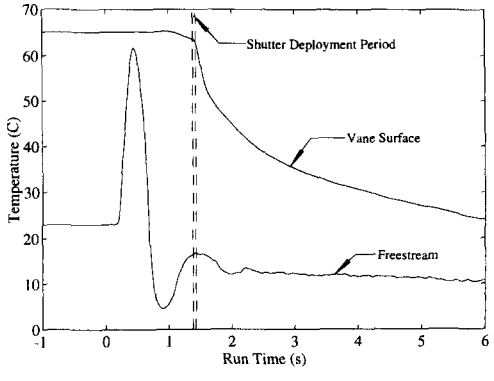

Figure 11 Thermocouple temperature histories

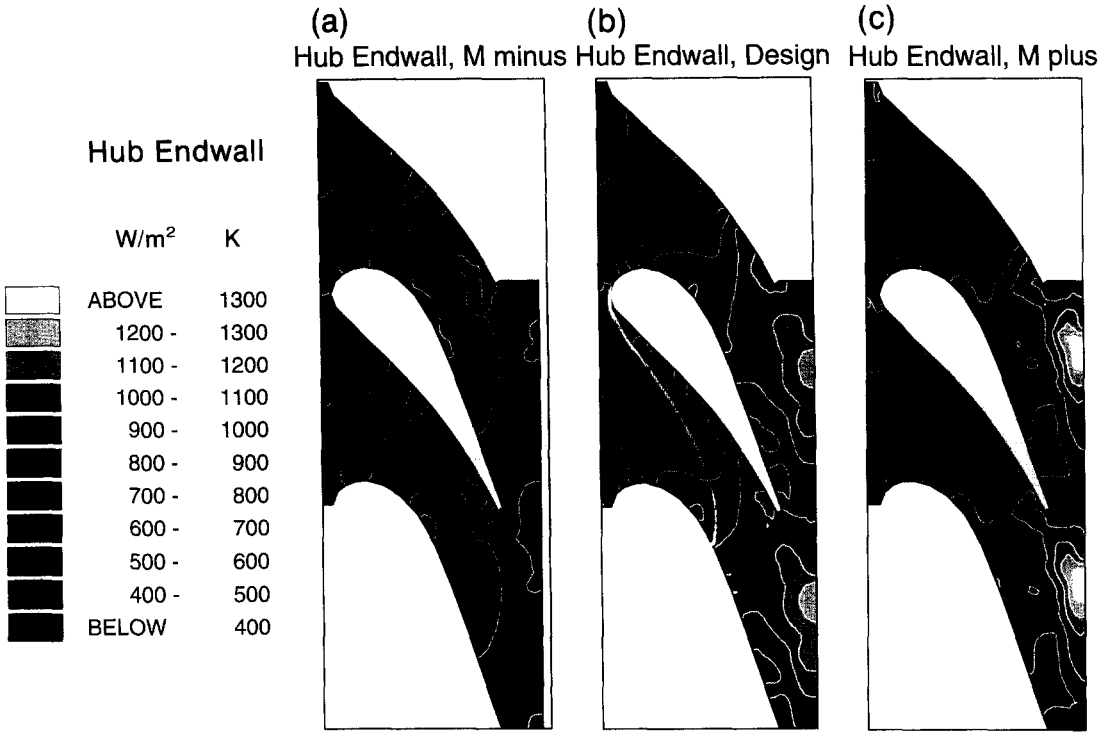

Figure 12 Heat transfer coefficient (W/m^2 K) contours on the hub endwall: (a) Mach minus; (b) design; (c) mach plus

curvature (i.e., hub leading-edge region), there is a slight distortion of the actual geometry. The end-wall contours follow the same general pattern reported by researchers using thin film gauge techniques on 3-D geometries but with greater spatial detail. The largest number of gauges used at engine-representive conditions (Harasgama and Wedlock 1990) were 35 on the hub and 39 on the casing endwalls. The maximum resolution for the image-processing system and from the camera positions that were

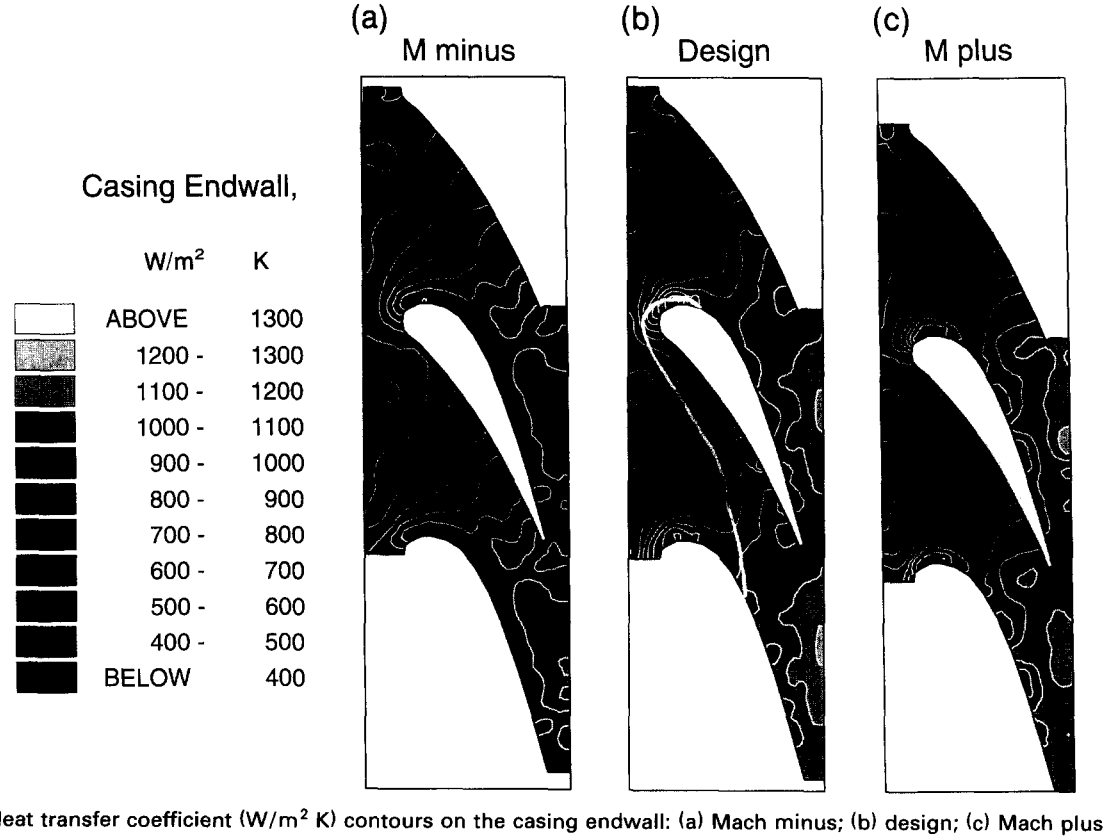

Figure 13 Heat transfer coefficient (W/m^2 K) contours on the casing endwall: (a) Mach minus; (b) design; (c) Mach plus

used in the experiments was over 5000 points. The contours in Figures 12 and 13 are made from over 200 measurements per endwall per passage. The measurement locations were not chosen from a regular grid: the measurement points were concentrated in the regions of high gradients in heat transfer, which are clearly visible from the video records. An increase in resolution did not significantly alter the contour patterns or introduce new flow features.

In all three cases, the heat transfer coefficient is seen to increase from the front to the back of the endwall as the flow accelerates. Generally, the heat transfer contours reflect those of Mach number. An exception occurs near the pressure surface downstream of separation line *a* (cross-flow region 2 in Figures 8 and 10), where the flow passing over the horseshoe vortex has impinged onto the endwall and partially stagnated. The streamlines are then swept across the passage towards the suction surface. Here there is a competing effect: the boundary layer is growing, which reduces the heat transfer, and the flow is accelerating (i.e., Mach number increasing), which increases the heat transfer. Near the trailing edge of the hub endwall, this results in higher heat transfer levels on the pressure side than the suction side, despite the higher Mach numbers in the latter location. On the casing endwall, these competing effects result in nearly equal heat transfer levels on the pressure and suction sides near the trailing edge. The competing effects provide an explanation for the characteristic V-shaped pattern in the contours. The separation lines (Figures 12b and 13b) are seen to align with the farthest penetration of the contours into the passage.

The casing end-wall contours illustrate an enhanced region of heat transfer on the suction surface side near the leading edge. This high heat transfer corresponds to the high levels found by Martinez-Botas et al. (1995) near the casing on the suction aerofoil surface. The high heat transfer is associated with the horseshoe vortex. The horseshoe vortex does not create a region of high heat transfer near the leading edge on the hub endwall, because the vortex has lifted off the endwall much closer to the stagnation point. This was discussed in the previous section and is clearly illustrated by the superimposed separation lines.

The heat transfer contours for the design, Mach plus, and Mach minus conditions all demonstrate similar patterns. The highest levels of heat transfer occur in the wakes and in the enchanced region near the leading edge on the casing endwall. There is a consistent trend in the shape of the contours near to and along the suction side of the endwall. This trend is that an area of low heat transfer penetrates farther downstream with increasing Mach number. The pressure gradient across the NGV and the radial pressure gradient within the passage increase with increasing exit Mach number. These gradients effect the secondary flow patterns and the position where the horseshoe vortex sweeps up onto the aerofoil surface, ultimately affecting the heat transfer contours.

Generally, the heat transfer levels have an uncertainty of approximately 10%. A discussion quantifying the uncertainty appears in the appendix.

Conclusions

The transient liquid crystal technique has been successfully used to measure global contours of heat transfer on the endwalls of an annular cascade of nozzle guide vanes. The measurements were performed at three engine representative Reynolds and Mach numbers. The free-stream turbulence intensity levels and length scales have been measured using a hot-wire anemometer and are also engine representative. The advantages of a full surface measurement technique has been demonstrated by the detail of the heat transfer contours measured. Aerodynamic measurements of Mach number distributions on the end-wall surfaces have also been presented, along with surface-shear flow visualisation using oil and dye techniques. The principal features of the heat transfer maps have been discussed with the aid of the secondary flow and Mach number patterns.

Acknowledgments

The authors would like to thank Rolls-Royce plc and the Defence Research Agency for funding this work and granting permission for publication. The authors are grateful for the assistance of M. L. G. Oldfield, N. W. Harvey, R. F. Martinez-Botas, Z. Wang, P. T. Ireland, and T. Godfrey.

Appendix: Uncertainty analysis and discussion

The heat transfer coefficient was measured over a range of 400–1200 Wm^{-2} K^{-}. This is a threefold range. With the transient technique employed, the heat transfer coefficients are proportional to the square root of time. This meant a ninefold variation in the colour change times used in the data reduction. In regions of extreme heat transfer, measurements from only one crystal were employed, as only one was visible. In regions of low heat transfer, the temperature drop reached only the first crystal. In regions of high heat transfer, the first crystal colour change time was too short to measure. In general, however, the heat transfer measurements from the two crystals were consistent.

Following Martinez-Botas (1993), uncertainty stems from five main sources: total temperature uncertainty (± 0.2 C from the thermocouple), ϵ_{gas}; crystal temperature calibration error (± 0.2 C), ϵ_{cry}; image-processing errors and errors associated with the shutter-opening time (taken as ± 0.1 s), ϵ_{time}; initial temperature uncertainty (± 2 C), ϵ_i; and an uncertainty associated with the thermal properties of the substrate material ($\sqrt{\rho ck} = 569 \pm 29$ Wm^{-2} K^{-1} $s^{0.5}$), ϵ_{sub}. The total uncertainty is taken as the root mean square value of the individual components. This uncertainty affects the heat transfer coefficient and is a function of the measurement time, hence, a function of the measurement location. Table A1 illustrates the magnitude of the error at the leading and trailing edges and at midchord along the midpassage streamline of the casing endwall.

One observes from the table that generally the largest contribution to the uncertainty in the heat transfer coefficient is the uncertainty in the thermal product, $\sqrt{\rho ck}$, for perspex. Errors in the measurements in regions with short colour change times (trailing-edge region) are strongly influenced by the time uncertainty associated with the start-up transient. However, the shutter-opening time is short enough that these uncertainties are limited.

The calculation of the heat transfer coefficient from the transient liquid crystal technique is based upon solving the one-dimensional (1-D) conduction equation with known boundary conditions. One condition is that the substrate material is to be at a uniform temperature. In the experiments reported here, this temperature is initially set to be uniform. However, because the heat transfer coefficient varies around the blade, the surface

Table A1 Uncertainty analysis

Location	ϵ_{gas}	ϵ_{cry}	ϵ_{time}	ϵ_i	ϵ_{sub}	Total
LE	1.0%	1.5%	1.2%	2.5%	8.0%	8.7%
50%	1.1%	1.6%	3.0%	2.6%	8.1%	9.2%
TE	0.8%	1.2%	9.1%	2.5%	8.1%	12.5%

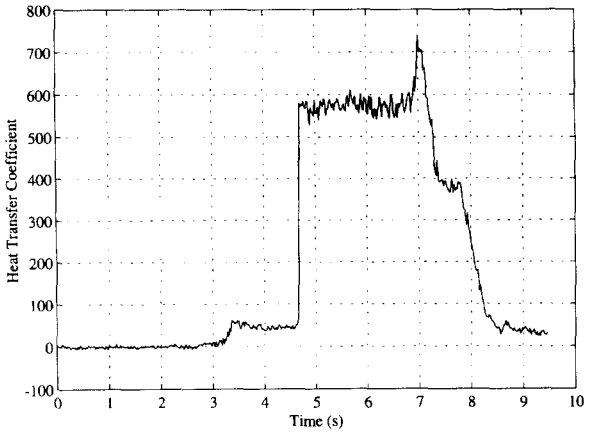

Figure A1 Heat transfer coefficient (W/m^2 K) history from thin film gauge

cools at different rates, and the substrate temperature is no longer uniform once the experiment begins. This nonuniformity in the thermal boundary conditions can affect the measurement of the local heat transfer coefficient, but this effect will be shown to be small.

To illustrate this, experiments have been performed using fast-response thin film gauges (Guo et al. 1995). Figure A1 shows a typical result from these experiments. The data were taken from a gauge on the blade aerofoil surface, and conditions were identical to those described in this paper. The thin film gauge yields a continuous history of the surface temperature, not just the value at two points, as is the case with two liquid crystals. This leads to continuous measurements of heat flux and heat transfer coefficient. The latter (in units of W/m^2 K) is shown in Figure A1. One observes that the heat flux from the leakage is small and that the heat transfer coefficient is constant with time, while the flow over the NGV is steady. The heat transfer coefficient measured at early times, when the substrate temperature is uniform, is very similar to that measured at later times, when the substrate temperature is nonuniform. This implies that the effect of nonuniformity in substrate temperature on local heat transfer coefficient is small in the case of the experiments reported here.

The roughness of surfaces coated with liquid crystals depends on whether the surfaces have been polished after the crystals have been sprayed. For the experiments reported here, the peaks in the surface roughness were approximately 25 μm. This roughness does have an influence on the heat transfer levels measured (Guo et al. 1995), but an investigation into this effect was not pursued in the work reported herein.

References

Ames F. E. and Moffat R. J. 1990. Effects of simulated combustor turbulence on boundary layer heat transfer. ASME HTD, 138

Chana K. S. 1992. Heat transfer and aerodynamics of high rim speed turbine nozzle guide vane with profiled end-walls. ASME Paper 92-GT-243

Fitt A. D., Forth C. J. P., Robertson B. A. and Jones T. V. 1986. Temperature ratio effects in compressible turbulent boundary layers. *Int. J. Heat Mass Transfer*, **29**, 159–164

Guo S. M., Spencer M. C., Lock G. D., Jones T. V. and Harvey N. W. 1995. The application of thin film gauges on flexible plastic substrates to the gas turbine situation. ASME Paper 95-GT-357

Harasgama S. P. and Wedlake E. T. 1990. Heat transfer and aerodynamics of a high rim speed turbine nozzle guide vane tested in the RAE isentropic light piston cascade (ILPC). ASME Paper 90-GT-41

Harvey N. W. 1991. Heat transfer on nozzle guide vane end walls. University of Oxford, DPhil thesis

Harvey N. W., Wang Z., Ireland P. T. and Jones T. V. 1989. Detailed heat transfer measurements in nozzle guide vane passages in linear and annular cascades in the presence of secondary flows. AGARD Paper CP-469

Harvey N. W. and Jones T. V. 1990. Measurement and calculation of end wall heat transfer and aerodynamics on a nozzle guide vane in an annular cascade. ASME Paper 90-GT-301

Hinze J. O. 1975. *Turbulence*. McGraw-Hill, New York

Kays, W. M. and Crawford M. E. 1993. *Convective Heat and Mass Transfer*. McGraw-Hill, New York

Kingcombe R. C., Harasgama S. P., Leversuch, N. P. and Wedlake, E. T. 1989. Aerodynamic and heat transfer measurements on blading for a high rim-speed transonic turbine. ASME Paper 89-GT-228

Langston L. S. 1989. Research on cascade secondary and tip-leakage flows — Periodicity and surface flow visualization. AGARD Paper CP-469

Martinez-Botas R. F. 1993. Annular Cascade Aerodynamics and Heat Transfer. University of Oxford DPhil thesis

Martinez-Botas R. F., Main A. J., Lock G. D. and Jones T. V. 1993. A cold heat transfer tunnel for gas turbine research on an annular cascade. ASME Paper 93-GT-248

Martinez-Botas R. F., Lock G. D. and Jones T. V. 1995. Heat transfer measurements in an annular cascade of transonic gas turbine blades using the transient liquid crystal technique. *J. Turbomachinery*, **117**, 425–431 (also ASME Paper 94-GT-172)

Moss R. W. and Oldfield M. L. G. 1991. Measurements of hot combustor turbulence spectra. ASME Paper 91-GT-351

Schultz D. L. and Jones T. V. 1977. Heat-transfer measurements in short-duration hypersonic facilities. AGARD Paper AG-165

Sieverding C. H. 1985. Recent progress in the understanding of basic aspects of secondary flows in turbine blade passages. *J. Eng. Gas Turbines Power*, **107**

Takeishi K., Matsuura M., Aoki S. and Sato T. 1989. An experimental study of heat transfer and film cooling on low aspect ratio turbine nozzles. ASME Paper 89-GT-187

Wang Z. 1991. The application of thermochromic liquid crystals to detailed turbine blade cooling measurements. University of Oxford, DPhil thesis